

# **Coherence of plasmon excitations in chemically heterogeneous nanoarrays**

Kevin Conley,<sup>†,‡</sup> Neha Nayyar,<sup>¶</sup> Tuomas P. Rossi,<sup>†,§</sup> Mikael Kuisma,<sup>||</sup>

Volodymyr Turkowski,<sup>¶</sup> Martti J. Puska,<sup>†</sup> and Talat S. Rahman<sup>\*,¶,†</sup>

<sup>†</sup>*Department of Applied Physics, COMP Centre of Excellence, Aalto University School of Science, P.O. Box 11100, FI-00076 Aalto, Finland*

<sup>‡</sup>*Department of Applied Physics, QTF Centre of Excellence, Aalto University School of Science, P.O. Box 11100, FI-00076 Aalto, Finland*

<sup>¶</sup>*Department of Physics, University of Central Florida, Orlando, Florida, USA*

<sup>§</sup>*Department of Physics, Chalmers University of Technology, SE-412 96 Gothenburg, Sweden*

<sup>||</sup>*Department of Chemistry, Nanoscience Center, University of Jyväskylä, FI-40014 Jyväskylä, Finland*

E-mail: talat.rahman@ucf.edu

## **Abstract**

The capability of collective excitations, such as localized surface plasmon resonances, to produce a versatile spectrum of optical phenomena is governed by the interactions within the collective and single-particle responses in the nite system. In many practical instances, plasmonic metallic nanoparticles and arrays are either topologically or chemically heterogeneous, which affects both the constituent transitions and their interactions. Here the formation of collective excitations in weakly doped nanoarrays is described using recently developed quantum mechanical methods. The additional impurity-induced modes in the optical response of gold nanoarrays doped

with Cu and Pd can be thought to result from intricate interactions between separated excitations or transitions. We investigate the heterogeneity at the impurity level, the symmetry aspects related to the impurity position, and the influence of the impurity position on the confinement phenomena. The chemically rich and symmetry-dependent quantum mechanical effects are analyzed with Transition Contribution Maps demonstrating the possibility to develop nanostructures with more controlled collective properties.

## Keywords

plasmonics, molecular plasmonics, time-dependent density-functional theory, transition contribution maps, collective excitation

## Introduction

The interaction of light with finite metallic nanoparticles and arrays can excite localized surface plasmon resonances (LSPR). The collective oscillation of electrons emerges from early descriptions of a degenerate electron gas.<sup>1</sup> Recently Time-Dependent Density Functional Theory (TD-DFT) methods are applied to increasingly large systems, such as Au<sup>2</sup> and Ag nanoparticles.<sup>3</sup> The prospect of manipulating the interaction among the electron-hole pairs within plasmons has motivated exploration for photocatalysis<sup>4</sup> or hot electron generation at metal-semiconductor interfaces.<sup>5,6</sup> Goal-oriented studies necessitate investigation of nanosystems which are not topologically or chemically homogeneous for their unique pathways of plasmon formation and decay. Introducing heterogeneity will affect the extended electronic structure and its coherent excitations.

Collective electron excitations, such as LSPRs in nanoparticles and so-called molecular plasmons in smaller atomic arrangements or molecules, can be analyzed as interactions between contributing electron-hole excitations. Indeed, the identification and analysis of the coherent electron-

hole contributions in excitation peaks of photoabsorption spectra has become easily attainable with analysis methods<sup>7,8</sup> alongside TD-DFT. A Transition Contribution Map (TCM) visually parses the energy of the individual electron-hole transition contributions and indicates the possible interactions between electron-hole pairs.<sup>8</sup> Plasmons and single-particle excitations are also differentiated by the distinct dependence on the Coulomb interaction scaling parameter,  $\lambda$ , in TD-DFT.<sup>7</sup> Moreover, the Generalized Plasmonicity Index is an analogous method to quantify the contributions from low energy transitions<sup>9</sup> which shows clearly the formation of the LSPR.<sup>10,11</sup>

TCMs are increasingly practical to analyze plasmonic systems, such as Ag and Al nanoparticles<sup>12,13</sup> and MoS<sub>2</sub> nanoflakes.<sup>14</sup> TCMs of the intense photoabsorption excitations have previously provided fundamental insight into how the individual electron-hole contributions are pieced together from the nodal structure of the delocalized sp-states within homogeneous metallic arrays of varying width.<sup>15</sup> The molecular plasmon has growing collectivity from coherent KS transition contributions.

Molecular plasmons exhibit effects from the finite-size quantum confinement, symmetry, and avoided crossings within nanosystems such as metallic clusters,<sup>16–18</sup> arrays,<sup>15,19,20</sup> and conjugated and aromatic hydrocarbons.<sup>21–23</sup> As evidenced by previous computational studies,<sup>15,19,20</sup> double chain metallic arrays contain many of the physical and chemical phenomena which are central to any molecular plasmon. They exhibit plasmonic excitations arising from a clearly identifiable nodal structure. Further the structures can be elongated (up to 5.5 nm in length) without needlessly increasing computational tractability. These advantages become clear when chemical heterogeneity changes the symmetry and electronic structure and resulting formation of molecular plasmons in nano-alloy arrays.

In this paper, we calculate the optical response of weakly doped free-standing atomic arrays using TD-DFT. First we briefly discuss the effects within homogeneous Au double chain arrays. Then we describe how the electronic structure and plasmonic features change when the arrays are weakly doped with either Cu or Pd. The geometries of the nanoarrays and the computational methods employed in the TD-DFT calculations and in their analysis are described in the Methods

section.

## Results and Discussion

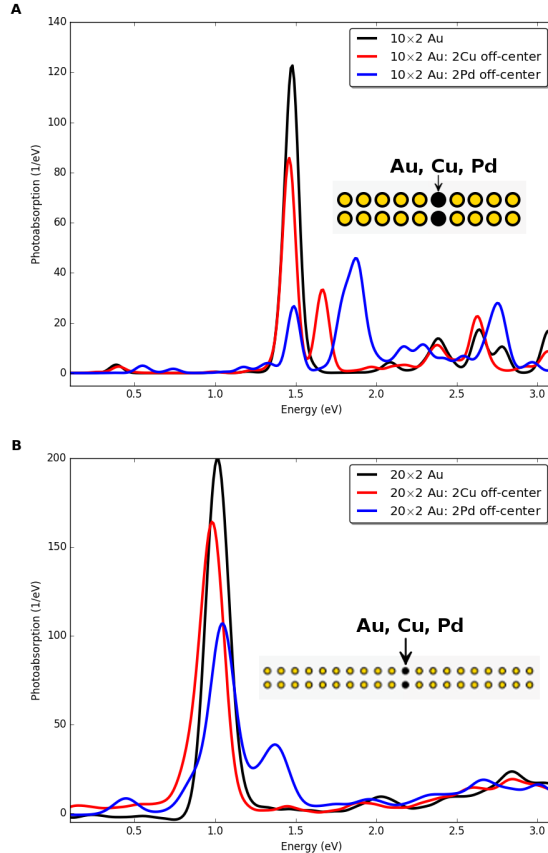


**Figure 1: Photoabsorption spectra of weakly doped double chain arrays.** Photoabsorption spectra of a  $10 \times 2$  (A) and  $20 \times 2$  (B) double chain Au array doped with Pd or Cu within the array compared to that of a corresponding pristine Au array. There is one impurity atom in each chain of the array and the impurities are nearest neighbors.

Nano-alloy arrays contain numerous physical and chemical aspects fundamental to molecular plasmonics in chemically heterogeneous systems. In this Section, the photoabsorption modes in the spectra of  $10 \times 2$  and  $20 \times 2$  arrays weakly doped with Cu or Pd (Figure 1) are described qualitatively. In the subsequent subsections, TCMs and the  $\lambda$ -evolution of the collective response

are used to examine the interactions among the electron-hole contributions and their influence on the plasmon formation.

Molecular arrays with varying number of chains have been examined elsewhere<sup>15,19,20</sup> and have a non-monotonic shift of the plasmon frequency due to the evolving subband structure and nodal planes. TCMs demonstrated the increase in the collectivity as the transitions within each contributing subband become more numerous.<sup>15</sup> Double chain Au arrays were shown to have a strong photoabsorption mode from predominantly the subband with zero longitudinal nodes across the array.<sup>15</sup> Classically the strong absorption can be associated to delocalized electrons of high density between two Au chains. Strong single peaks are seen in Figure 1 for the absorption spectra of the  $10 \times 2$  and  $20 \times 2$  arrays which are the basic model systems considered in this manuscript.

Elongating the arrays will modify the subband structure and shift the plasmon frequency. The  $10 \times 2$  Au array has an intense photoabsorption mode at 1.48 eV as seen in Figures 1(A, black line) and 2. The photoabsorption mode red-shifts to 1.01 eV in the elongated  $20 \times 2$  array as seen in Figures 1(B, black line) and 3.

Introducing chemical heterogeneity to the Au array by doping can shift the energy of the mode or generate additional strong photoabsorption modes. For example, a clearly resolved split of the plasmon mode is observed when Cu is doped within the small array (Figure 1A). The modes coalesce into an unresolved strong mode by lengthening the Cu-doped array (Figure 1B). The situation is different for Pd-doped arrays; two or more additional peaks form irrespective of the array length. This behavior differs qualitatively also from the case where a whole chain of Pd atoms replaces a chain of Au atoms in a mixed double-chain array, *i.e.*, the Pd row quenches the plasmon of the Au double chain.<sup>15</sup>

In the following sections, we discuss how the plasmonic features of Cu- or Pd-doped Au arrays are determined by their electronic structures and point group symmetries. The hybridization of states in nanoscale particles and quantum coherent interactions within the homogeneous and chemically heterogeneous arrays are identified and characterized using TCMs, Group Theory, and the  $\lambda$ -scaling approach.<sup>7</sup> The main features of the photoabsorption spectra of the nanowire sys-

tems were similar when calculated using Gaussian 03<sup>24</sup> with a B3PW91 hybrid functional<sup>25–27</sup> and a LanL2DZ basis set.<sup>28</sup> With the exception of the photoabsorption spectra calculated using Gaussian 03 shown in the Supporting Information, all the results presented and analyzed in this paper are obtained with the LCAO-TD-DFT method using the GPAW code<sup>12,29–31</sup> (See also the Methods section).

## Homogeneous array

In this subsection, the plasmon formation within homogeneous Au arrays is described using TD-DFT methods and TCMs of the Kohn–Sham transition contributions. The symmetry and interaction between the transition contributions in the chemically pure arrays forms the basis of the later discussion of chemically heterogeneous systems.

The undoped  $10 \times 2$  Au double chain array has a single intense mode at  $\omega = 1.48$  eV and the construction of the electronic excitation from the individual KS transition contributions is illustrated in the TCM in Figure 2A. The electronic excitation consists of a contribution from the KS transition between sp-delocalized states with 6 and 7 transverse nodes,  $v_{6 \rightarrow 7}$  or  $(6,0) \rightarrow (7,0)$  wherein  $(t,l)$  denotes the number of transverse,  $t$ , and longitudinal,  $l$ , nodes. This contribution is shown as strong red dot on the TCM with the energy eigenvalues of the occupied ( $\varepsilon_o$ ) and unoccupied ( $\varepsilon_u$ ) states on the (vertical) horizontal axis. The transition is clearly below the line  $\varepsilon_u - \varepsilon_o = \omega$  which reflects the increase of the excitation energy due to the Coulomb and exchange-correlation kernel interactions. The KS orbitals of the initial and final states are shown adjacent to the TCMs. In double chain arrays, the transitions within other subbands are weak due to the presence of a longitudinal node between the two chains. Nevertheless, the HOMO  $\rightarrow$  LUMO transition, i.e.  $(2,1) \rightarrow (3,1)$ , has a minor contribution and is dimly visible in the lower right corner. The transverse nodal difference of both contributing transitions is unity. This coherence produces a dipolar total induced density of the collective excitation is dipolar as shown in the TCM inset.

The evolution of the photoabsorption spectra with the interaction strength parameter,  $\lambda$ , is shown in Figure 2B. See Equation 2 in the Methods section for details. A dark red stripe originat-

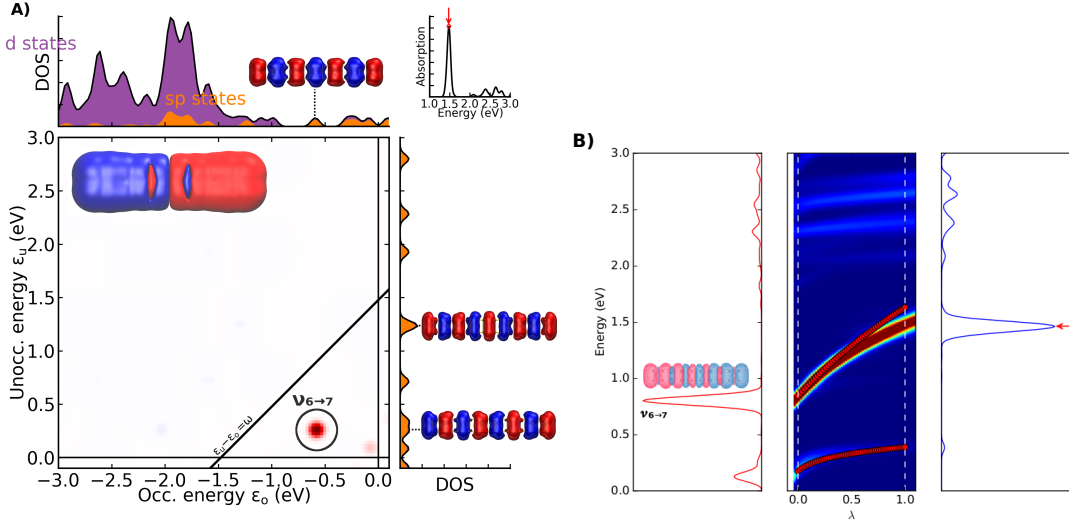


Figure 2: **Homogeneous  $10 \times 2$  Au array.** A) Contributions to the plasmonic excitation at  $\omega = 1.48$  eV. B)  $\lambda$ -dependent photoabsorption spectra of the array. The red dots denote the  $\lambda$ -dependent pseudo-excitation energies of two interacting KS transitions ( $v_{6 \rightarrow 7}$  and the HOMO  $\rightarrow$  LUMO). The arrow indicates the photoabsorption mode analyzed in the TCM.

ing at  $v_{6 \rightarrow 7}$  blue-shifts as  $\lambda$  increases. This shift has been used to indicate plasmonicity in similar atomic arrays and molecules.<sup>7,10,21,22</sup> The mode formed by the weaker HOMO  $\rightarrow$  LUMO transition, initially at 0.17 eV, gradually diminishes while blue-shifting with increasing  $\lambda$ . The light horizontal stripes around 2 eV are formed by the interband transitions from the d-band. These transitions are marginally affected by the interaction parameter indicating single-particle character.

The interaction between specific KS transitions can be examined by renormalizing the excitation energies of a subset of KS transitions for different interaction strength parameters. See Equation 2 in the Methods section for details. The  $\lambda$ -evolution of the pseudo-excitation energies from the interaction between  $v_{6 \rightarrow 7}$  and the HOMO  $\rightarrow$  LUMO is drawn as red dots in Figure 2B. The collective effect of the two KS transitions generates two pseudo-excitation energies which blue-shift to about 0.5 and 1.5 eV when  $\lambda = 1$ . The transfer of energy to the background of the other KS transitions leads to a minor discrepancy between the pseudo-excitation energies at  $\lambda = 1$  and the spectra with the full set of all possible KS transitions (Figure 2B, right panel).

Elongating the double chain array to  $20 \times 2$  red-shifts the intense photoabsorption mode to 1.01 eV. The transition energy (eigenvalue difference of the KS states in the transition) of the

dominant contribution to the molecular plasmon decreases in the longer homogeneous array. In the  $10 \times 2$  array, the first order, fundamental transition, *i.e.* having  $\Delta n = 1$  and zero longitudinal nodes, is  $(6, 0) \rightarrow (7, 0)$ . Whereas in a  $20 \times 2$  array the fundamental transition occurs from the  $(13, 0)$  to the  $(14, 0)$  KS orbital (Figure 3A). The transition energies are consistent with those of a non-interacting homogeneous electron gas, which has been discussed for molecular plasmons elsewhere.<sup>7</sup> In TCMs the decrease of the transition energies in longer arrays manifests as a shift of the contribution toward the lower right corner.

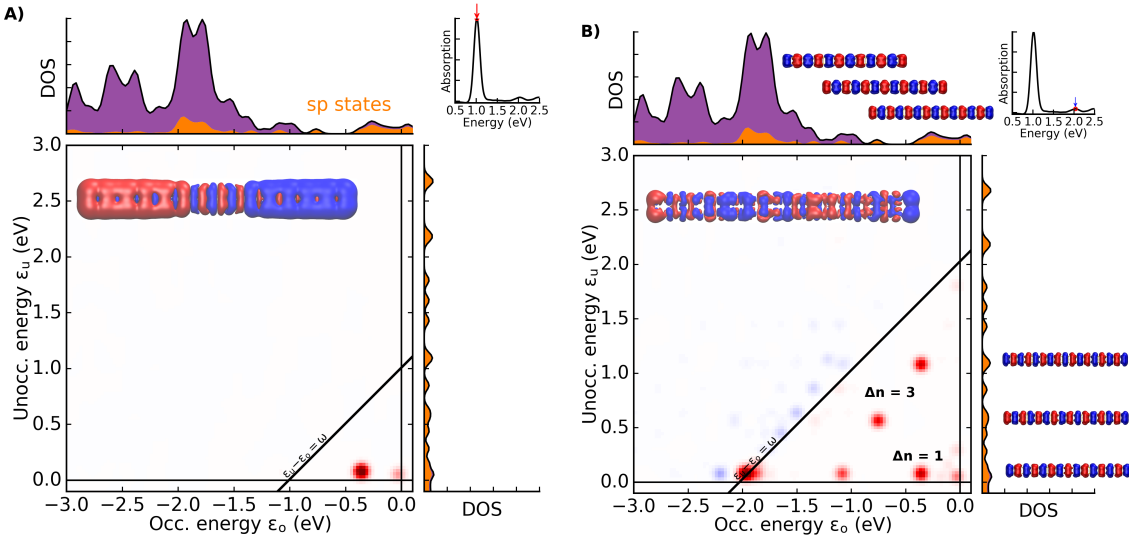


Figure 3: **Homogeneous  $20 \times 2$  Au array.** TCM of the photoabsorption excitations at (A) 1.01 and (B) 2.03 eV.

The decreased energy spacing of the sp-delocalized states in the longer arrays can be observed in the DOS alongside the respective TCMs. For example, the virtual sp-states are more dense in the longer array than the well-separated states in the shorter array. The KS orbitals  $(8, 0)$  and  $(15, 0)$  of the  $10 \times 2$  and  $20 \times 2$  array have been identified in the TCMs in Figures 2A and 3B, respectively.

Even order transitions in the centrosymmetric arrays are parity forbidden. Dipole forbidden dark modes, such as the second order  $v_{6 \rightarrow 8}$  in the homogeneous  $10 \times 2$  array, are absent in the non-interacting spectrum (Figure 2B, left panel). The three possible third order transitions, however, are parity-allowed. These higher order transitions are visible in the TCM when they mix with the inter-band single-particle excitations at higher energies. For example the TCM at 2.03 eV is shown

in Figure 3B.

## Cu-doped array

In this subsection chemical heterogeneity is introduced to the homogeneous Au arrays by substituting one Au in each chain with Cu (See Figure 1). We first explain the symmetry dependent influence of the chemical heterogeneity on the electronic structure and how doping introduces higher order transitions. Then we analyze the interaction between the multi-order KS transitions *via* Coulombic interactions and consequence on the coherent collective excitations.

Doping a  $10 \times 2$  Au array with Cu off-center produces two photoabsorption modes at 1.46 and 1.66 eV as seen in Figure 1B. The construction of the electronic excitation in the higher energy excitation in the doped array is illustrated in Figure 4A. See Figure S1A for the TCM of the lower energy mode of the doped array. Like the homogeneous array discussed above, the Cu-doped array hosts a KS transition between sp-delocalized states with 6 and 7 transverse nodes, *i.e.*  $v_{6 \rightarrow 7}$ . The KS transition,  $v_{6 \rightarrow 7}$ , shown in the TCM, strongly contributes to both excitations of the doped array.

In addition, there are contributions from two additional transitions, labelled  $v_{5 \rightarrow 7}$  and  $v_{6 \rightarrow 8}$ . These contributions are from second order transitions between the sp-delocalized states,  $(5, 0) \rightarrow (7, 0)$  and  $(6, 0) \rightarrow (8, 0)$ . There are no corresponding KS transitions in the pure array as they are dipole-forbidden dark transitions in the centro-symmetric array. By being positioned off-center the Cu dopants break the symmetry of the pure array and change the point group from  $D_{2h}$  to  $C_{2v}$  and transitions between states with an even number difference in transverse nodes are no longer dipole-forbidden.

The effect of the dopants on the initial and final wavefunctions of  $v_{5 \rightarrow 7}$  are depicted in Figure 4C, left.  $\psi_{(5,0)}$  and  $\psi_{(7,0)}$  of the homogeneous and Cu-doped array are plotted 3 Å off the array edge and in the plane of the array. The sinusoidal pattern depicts the 5 and 7 transverse nodes of the sp-delocalized states. Doping the array breaks the symmetry of the magnitude of the wavefunctions along the array axis, *i.e.* along the direction of the external electric field, while maintaining the nodes. This is also observed in the respective KS orbitals in Figure 4C, center. The partial

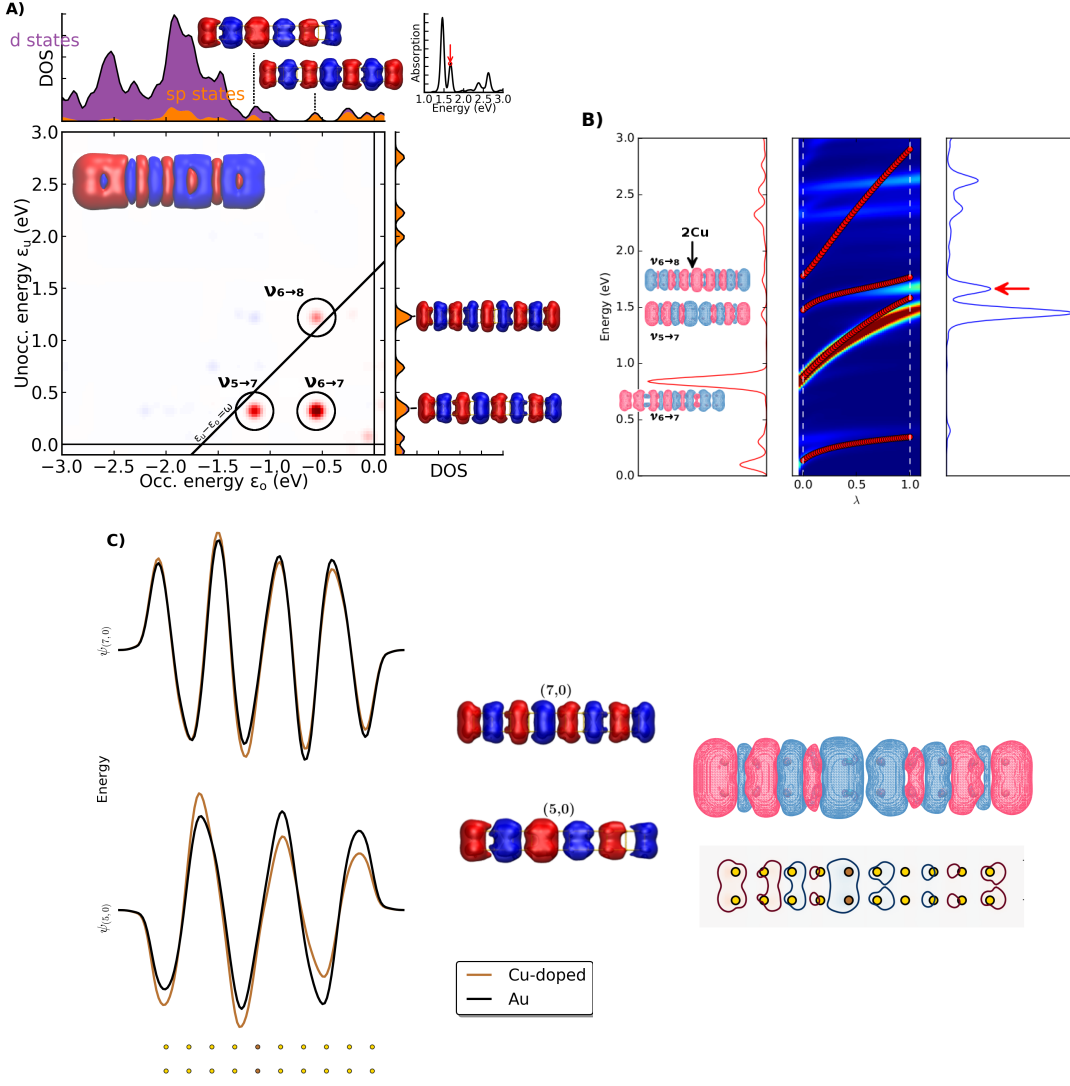


Figure 4: **Off-center Cu-doped  $10 \times 2$  array.** There is one impurity atom in each chain and the impurities are nearest neighbors as shown in Figure 1. A) Contributions to the doping induced photoabsorption mode at  $\omega = 1.66$  eV. B)  $\lambda$ -dependent photoabsorption spectra of the Cu-doped array. The arrow indicates the photoabsorption mode analyzed in the TCM. C) Wavefunctions of the  $(5,0)$  and  $(7,0)$  states in homogeneous and Cu-doped  $10 \times 2$  Au array (left). The respective KS orbitals and partial transition density of the Cu-doped array are shown in the center and right panels.

transition density between these states is given in Figure 4C, right as a 3D representation (top) and as a slice 0.75 Å above the plane of the array (bottom). There is an overall dipole because the magnitude on the left side of the array is greater than that on the right side of the array.

Two additional weak modes from  $v_{5 \rightarrow 7}$  and  $v_{6 \rightarrow 8}$  appear in the non-interacting spectrum in the left panel of Figure 4B. Each mode occurs at the energy corresponding to the respective eigenvalue difference of the KS states in the transition ( $\Delta\epsilon = 1.47$  and 1.78 eV). The magnitudes of  $v_{5 \rightarrow 7}$  and  $v_{6 \rightarrow 8}$  are weak relative to that of  $v_{6 \rightarrow 7}$ , which is the strong mode at  $\Delta\epsilon = 0.88$  eV. The large overall dipole moment of  $v_{6 \rightarrow 7}$  is evident in the well-separated partial induced density shown adjacent to the non-interacting spectrum.  $v_{5 \rightarrow 7}$  and  $v_{6 \rightarrow 8}$  have weak dipole moments due to the even order of the transitions.

Once the even order KS transitions have been become parity-allowed through the doping, they can interact with fundamental KS transition. The evolution of the doped photoabsorption spectra with the interaction strength parameter is shown in Figure 4B. Similar to the homogeneous array, there is a strong blue-shifting mode originating at  $v_{6 \rightarrow 7}$ . The interactions among the KS transitions lead to a gradual brightening of the additional mode at a higher energy indicated by an arrow in Figure 4B. The resulting excitations consisting of mixed KS transitions are examined below using the TCMs and within the Casida framework.

Transitions  $v_{5 \rightarrow 7}$  and  $v_{6 \rightarrow 8}$  lie below and above the line at  $\omega = 1.66$  eV, respectively. The position reflects the energy of the photoabsorption mode ( $\omega$ ) relative to the difference of the eigen-energies of the initial and final states of the KS transition, i.e.  $\Delta\epsilon$ . It can be seen easily by comparing the non-interacting ( $\lambda = 0$ ) and fully interacting ( $\lambda = 1$ ) spectra in Figure 4B. The energy of  $v_{5 \rightarrow 7}$  in the non-interacting spectra is less than 1.66 eV and thus it lies below the  $\omega$ -probe line in the TCM. Similarly the contribution of  $v_{6 \rightarrow 8}$  to the excitation at 1.66 eV lies above the  $\omega$ -probe line.

The photoabsorption bands at 1.46 and 1.66 eV are collective excitations of multi-order KS transitions *via* Coulombic interactions. The second order transitions are not single-particle excitations despite the proximity of their contributions to the  $\omega$  probe-line. The collectivity of the

excitations is validated by inspecting the interaction among the KS transition contributions identified by the TCM.

The interaction strength or “coupling constant” between each electron-hole contribution pair is given by the off-diagonal matrix elements in  $K_{ia,jb}$  (See Equation 2). All KS transitions of the subset have  $A_1$  symmetry and interact, and yet the interaction is stronger among the KS transitions with the same order, *i.e.* between the two first order transitions (having either zero or one longitudinal node) and the two second order transitions. This pairing is demonstrated in the  $\lambda$ -evolution of the pseudo-excitation energies of smaller subsets of KS transitions given in Figure S2. For example, when the subset is restricted to only  $v_{5 \rightarrow 7}$  and  $v_{6 \rightarrow 8}$  (Figure S2, red circles), the two pseudo-excitation energies, formed by symmetric and anti-symmetric combinations of  $v_{5 \rightarrow 7}$  and  $v_{6 \rightarrow 8}$ , strongly diverge as  $\lambda$  approaches 1. On the other hand, there is little divergence in the pseudo-excitation energies of the symmetric and anti-symmetric combinations of  $v_{5 \rightarrow 7}$  and  $v_{6 \rightarrow 7}$  (Figure S2, white circles). This demonstrates that  $v_{5 \rightarrow 7}$  interacts more strongly with the other second order transition than with the first order transition.

The weak coupling of  $v_{6 \rightarrow 7}$  and  $v_{5 \rightarrow 7}$  is insufficient to produce the excitation at 1.66 eV. It is necessary to have both the strong pairing between the second order transitions and the weak interaction with the first order transition contributions. The multi-order interactions among the electron-hole contributions are contained within the subset consisting of all the KS transitions identified in the TCM ( $v_{5 \rightarrow 7}$ ,  $v_{6 \rightarrow 8}$ ,  $v_{6 \rightarrow 7}$  and the HOMO  $\rightarrow$  LUMO). The  $\lambda$ -evolution of the pseudo-excitation energies is drawn as red dots in Figure 4B and better reconstitutes the energies of the excitations in the spectra with full interaction (Figure 4B, right panel).

We now turn to the longer  $20 \times 2$  array containing off-center Cu dopants. The second order transitions,  $\Delta n = 2$ , are dipole active like those in the shorter Cu-doped array. This array will demonstrate the effect of reducing the energy difference between the interacting first and second order KS transitions. The energy spacing between the orders of the longer array follows from the discussion of homogeneous arrays and is validated by inspection. The energy gap in the 20 atom long double chain array is narrow enough that rather than manifesting as an well resolved

additional peak, the higher energy mode, induced by the symmetry break, coalesces into the main excitation mode. Thus, a single intense mode forms at 0.98 eV.

Again, contributions from second order transitions are visible in the TCM of the molecular plasmon in Figure 5A. We validate that these are indeed contributions from second order KS transitions by showing the respective KS orbitals adjacent to the TCM in Figure 5B. The two moderately intense peaks at 0.82 and 0.90 eV in the spectrum with  $\lambda = 0$  in Figure 5C correspond to  $\nu_{12 \rightarrow 14}$  and  $\nu_{13 \rightarrow 15}$ .

The excitation is formed by the collective interaction of transitions with different orders. The added contribution from the second order transitions does not significantly change the coherence of the well-separated total induced density from the homogeneous array as seen in the TCM insets. A more drastic effect is observed in the asymmetric lineshape of the mode. The photoabsorption on the low energy shoulder is formed by the plasmon splitting between the first and second order transitions. See the TCM at 0.83 eV in Figure S1B in which the second order contributions to the photoabsorption intensity are negative.

The loss of symmetry is also displayed when the low energy excitations mix with the interband single-particle excitations at higher energies. A 1-2-3 pattern from the first, second, and third order transition contributions is revealed in the TCM of a less intense mixed mode at 1.90 eV in Figure 5B. The pattern expresses the number of possible transitions within each order and increases according to Pascal's triangle in a 2D system. The dipole forbidden second order transitions are absent in the homogeneous  $20 \times 2$  Au array as demonstrated in the TCM at 2.03 eV (Figure 3B).

Centro-symmetric Cu-doped arrays present a unique situation in which the array is doped but has a transverse mirror plane and belongs to the  $D_{2h}$  point group. We demonstrate this in a 19 atom long double chain array. As expected, the second order transitions are dipole inactive and are absent in the TCM of the molecular plasmon at 1.05 eV as seen in Figure S3A. For comparison the molecular plasmon within a homogeneous array at 1.06 eV is shown in Figure S3B.

The situation of dopants placed within the arrays contrasts to the arrays formed with mixed homonuclear chains which are considered in detail elsewhere.<sup>15</sup> Both doped arrays have  $C_{2v}$  sym-

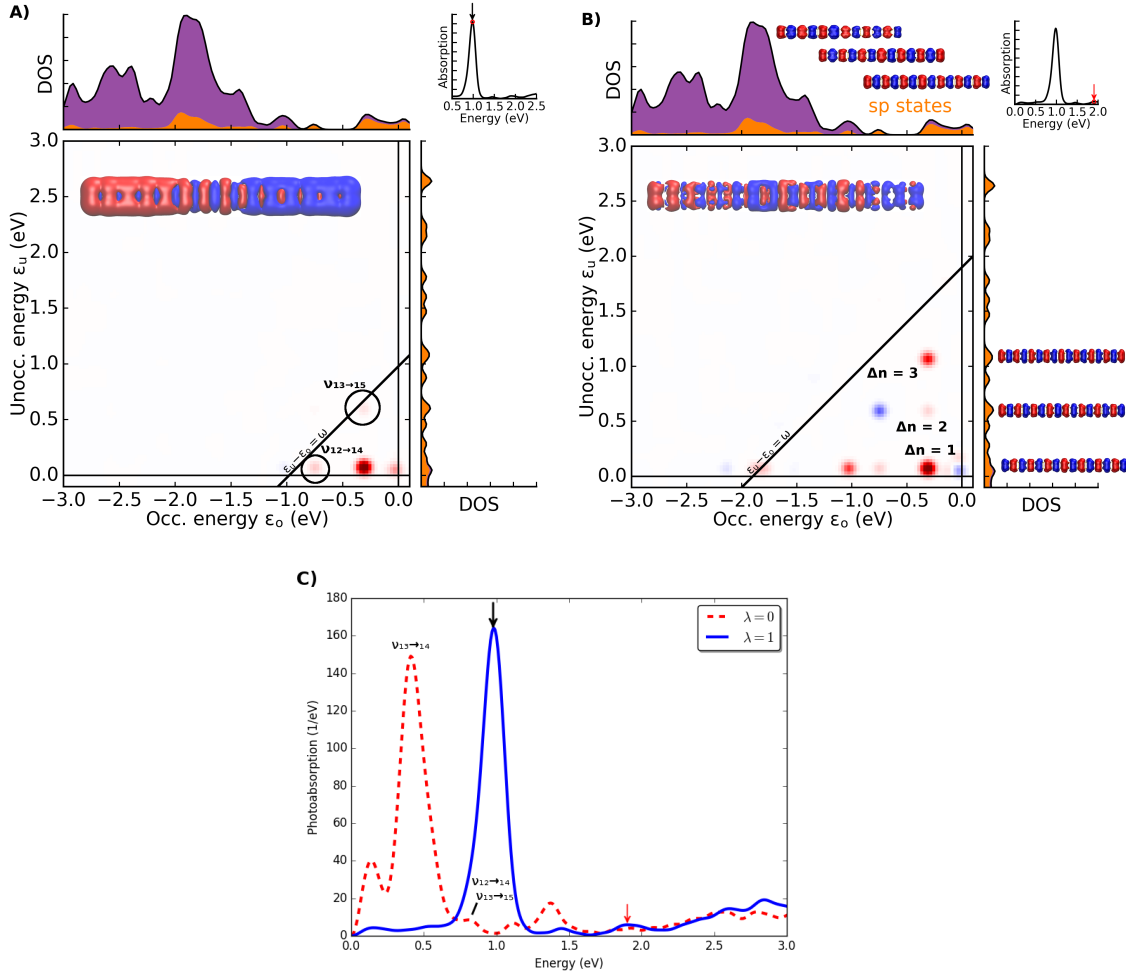


Figure 5: **Off-center Cu-doped  $20 \times 2$  Au array.** There is one impurity atom in both chains and the impurities are nearest neighbors. TCM of the photoabsorption excitations at  $\omega =$  (A) 0.98 and (B) 1.90 eV. C) Non-interacting and fully interacting photoabsorption spectra.

metry, but in mixed arrays, the chemical heterogeneity is not along the axis of the external electric field causing the transition dipole moment of the higher order modes along this axis to be negligible. This is similar to the situation when the Cu dopants are placed at the end of the array. Then the even order KS transitions,  $(5,0) \rightarrow (7,0)$  and  $(6,0) \rightarrow (8,0)$ , are allowed, but their oscillator strengths are very weak as seen by the absence of even order modes in the non-interacting spectrum in Figure S4.

## Pd-doped array

The type of chemical heterogeneity affects the electronic structure of the molecular array. Doping with Pd introduces d-states near the Fermi level which hybridize with the sp-delocalized states. Weak doping is sufficient to construct new photoabsorption modes as seen in Figure 1. In this subsection, we show that the decoherence of the modes is initiated by the sd-hybridization and coupling to higher order transitions.

The long  $(20 \times 2)$  Au array doped off-center with Pd (Figure 1B) has an intense photoabsorption mode at 1.04 eV with a low energy shoulder and a weaker but very clearly resolved mode at 1.37 eV. As described above, the higher order modes are closer in energy to the fundamental transition in an array of this length. Select KS orbitals are given in Figure S5B, and for convenience the order has been identified within the TCM in Figure 6B. It is clear the TCMs do not exhibit the same 1-2-3 pattern from the first, second, and third order transition contributions as in the case of the Cu-doped array. The s(p)d-hybridization between the Pd d-states and the Au sp-states increases the number of possible KS transitions within the each order and increases the collectivity.

Notably, the TCMs indicate that there are contributions from the even order transitions. Consistent with the discussion above, the point group of the array doped off-center with Pd changes to  $C_{2v}$ . A weak mode from the KS transitions with  $\Delta n = 2$  appear at about 0.8 eV in the non-interacting ( $\lambda = 0$ ) photoabsorption spectra in Figure 6C. This energy corresponds to the low energy shoulder in the spectrum with full interaction ( $\lambda = 1$ ) indicating that the active even order transition contributions split the plasmon. This is confirmed by a change in the sign of the second

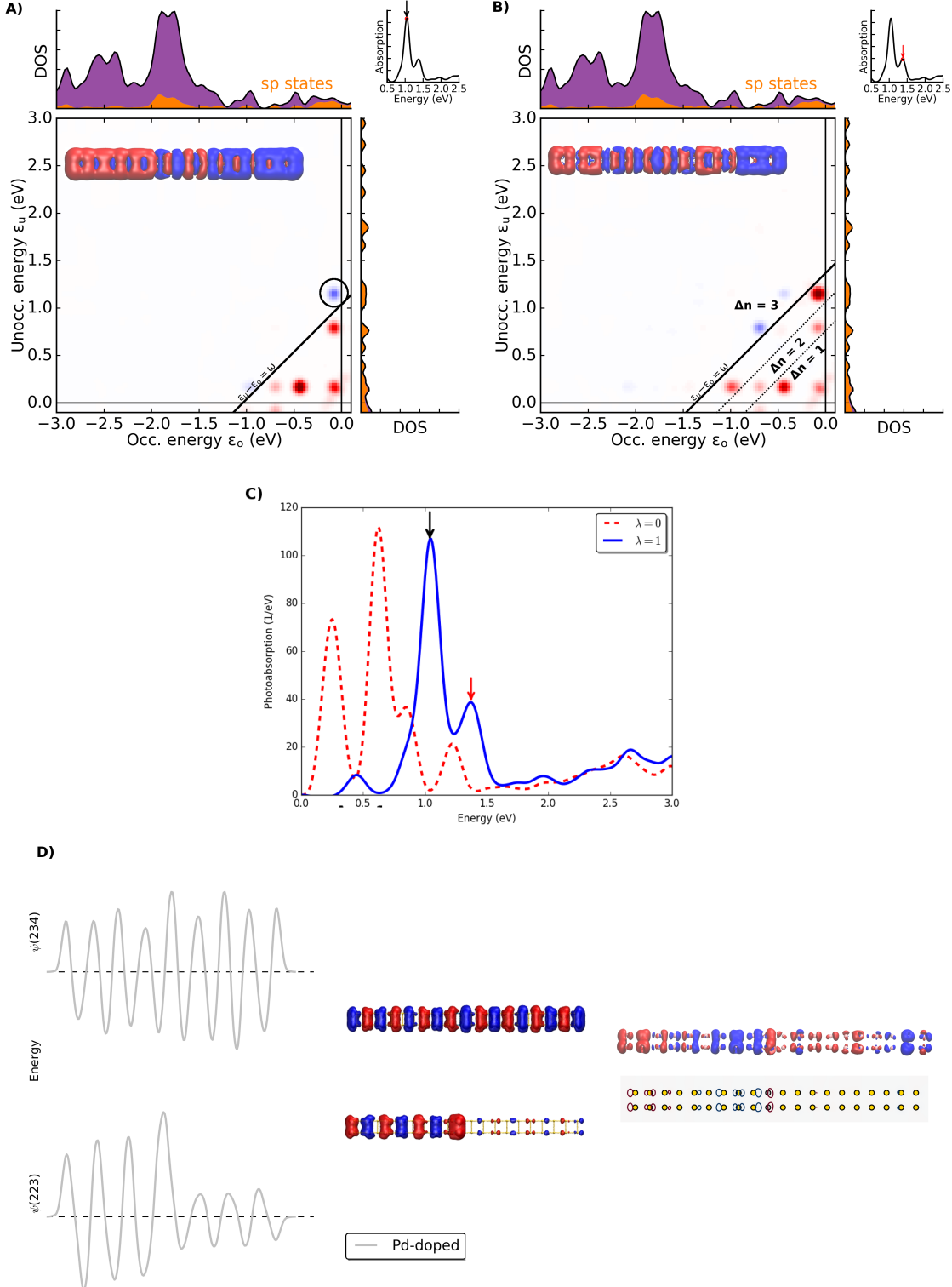


Figure 6: **Off-center Pd-doped  $20 \times 2$  Au array.** There is one impurity atom in both chains and the impurities are nearest neighbors. TCM of the photoabsorption excitations at (A) 1.04 and (B) 1.37 eV. The contribution from the circled transition ( $\psi(223) \rightarrow \psi(234)$ ) changes sign between these two excitations. C) Non-interacting and fully interacting photoabsorption spectra. D) Wavefunctions of  $\psi(223)$  and  $\psi(234)$  along the chain axis adjacent to the array (left). The respective KS orbitals and partial transition density are shown in the center and right panels.

order transition contributions at 0.80 eV (See TCM in Figure S5A). Such even order transitions and low energy shoulder are not observed in a centro-symmetric Pd-doped array.

The moderately intense mode at higher energy (1.37 eV) consists of contributions from the third order transitions (Figure 6B). Participation from the third order transitions was not observed in the homogeneous or Cu-doped arrays. Next we analyze one transition contribution to verify that the transitions are interacting to enhance the higher energy excitation.

The excitation at 1.37 eV lies just above the second and among the third order transition contributions. Some of the third order third order transition contributions change sign between the modes at 1.04 and 1.37 eV rather than existing as a fleeting single particle transition on the  $\omega$ -probe line. The change in sign occurs while the low energy transitions remain unchanged. One such transition contribution is circled in Figure 6A. This behavior has previously been described as strong coupling between a transition contribution (corresponding to the circled one in Figure 6A) and the plasmon in the case of a Ag<sub>55</sub> nanoparticle.<sup>8</sup> The interactions fragment the plasmon into anti-symmetric and symmetric combinations of transitions.<sup>32</sup> Here we demonstrate the ability of sd-hybridization to access the higher order odd transitions in two-dimensional nanosystems.

Within the array, sd-hybridization can localize the electron density of a given orbital predominately on either side of the array. KS transitions occur between these states and they participate in the collective excitations.  $\psi(223)$  and  $\psi(234)$  are plotted along the chain axis adjacent to the array in Figure 6D (left). The notation is changed from the homogeneous and Cu-doped array because of the complications due to the sd-hybridization. Away from the array edge the orbitals have 13 and 16 transverse nodes, respectively. The nodes are also observed in the corresponding isosurface plots in Figure 6D (center). It is clear that the amplitude of  $\psi(223)$  is larger on the left end of the array, and consequently the partial induced density will also be stronger on the left end Figure 6D (right).  $\psi(223) \rightarrow \psi(234)$  is just one contribution of the collective excitation and does not localize the total transition density of the plasmon completely. The contribution from the third order transitions is reflected in the increase of the internal nodes in the total induced density. The ends of the array continue to have the opposite charges.

The effect of the Pd remains strong even when the dopant is placed at the end of a small array. This is because the d-character near the Fermi level can induce a transition dipole even at the end of an array. The effect is lost in an elongated array because the third order transitions have a weak dipole moment. Details are provided in the SI and Figures S6 and S7.

## Conclusions

We have demonstrated how the coherent plasmon formation in atomic arrays doped with Cu or Pd is influenced by symmetry and hybridization induced coupling to higher order transitions using TD-DFT methods. The extended length and simplified nodal structure of double chain arrays makes identification straightforward and yet the electronic and optical properties of chemically heterogeneous atomic arrays are more tangled than a single chain doped with a transition metal<sup>33</sup> and arrays of mixed homonuclear chains.<sup>15</sup>

The generation of additional dipole-allowed transitions is dependent on the chemical composition, position, and symmetry of the doped atomic array. The collective interactions among the KS transitions produce composite photoabsorption modes. Cu dopants activate even order KS transitions which are also strongly dependent on  $\lambda$ . The anti-symmetric and symmetric combination with the first order transitions produces a new photoabsorption mode. The modes coalesce in elongated arrays due to the narrowed energy difference of the anti-symmetric and symmetric combinations.

Pd dopants allow the fundamental transitions to interact with the higher order transitions. In the off-center Pd doped  $20 \times 2$  Au arrays third order transitions participate in collective excitations. This access increases the plasmon fragmentation and the internal nodes within the induced density. Similar coupling between transitions has been observed in Ag nanoparticles in which a coherent induced dipole emerges from the interaction between confined transitions within a small homogeneous nanoparticle.<sup>8</sup> Here the collective effects and access to sd-hybridized transition with localized character are demonstrated in long two-dimensional systems with doping.

Inclusion of the Coulombic interactions among the transitions enables the identification of the low-energy electronhole transitions, and yet it does not show their coherence, an important characteristic of molecular plasmons. Here we demonstrate the alteration of the quantum coherence of the nascent plasmon by the participation of transitions with different orders. In addition, the chemical heterogeneity changes the electronic structure and orbital hybridization, which dictate the plasmon formation and decay processes. The aspects in doped two-dimensional nanoarrays can be applied more generally to other chemical heterogenous materials, such as metal nanoparticles with adsorbed molecules or ligands, structural defects, or at an interface.

## Methods

Gold (Au) atomic wires are constructed 10 to 20 atoms in length. One atom in the chain is doped by substituting either a noble metal (Cu) or transition metal (Pd) at different positions along the chain, and then two similar chains are assembled to form arrays of heteronuclear chains up to 5.5 nm long. See Figure 1. To mimic supported nanostructures and to allow a clear identification and analysis of the nodal structure and discrete electron-hole transitions, a square lattice is assumed and the bond length is set to 2.89 Å, as measured in experimentally realized Au chains on the NiAl(110) substrate.<sup>34</sup>

The electronic structure of the free-standing doped nanostructures was calculated with DFT<sup>35,36</sup> using the solid-state modified GLLB-SC exchange-correlation potential<sup>37</sup> which accurately describes the energy level positions of the d-states in noble metals.<sup>38,39</sup> We employ the GPAW code package<sup>12,29–31</sup> based on the projector-augmented wave (PAW) method<sup>40</sup> and utilize the ASE package.<sup>41</sup> Electronic wavefunctions are expanded as linear combinations of atomic orbitals (LCAO)<sup>42</sup> and occupied with less than 0.05 eV Fermi-Dirac smearing. The pseudo wavefunctions are evaluated in real space with a grid spacing of 0.3 Å and the electron density and potentials are evaluated with a grid spacing of 0.15 Å. The arrays are surrounded by at least 6 Å of vacuum and the Hartree potential is evaluated on a larger and coarser grid with at least 48 Å of

vacuum.

The optical response of the  $10 \times 2$  arrays was calculated within the LCAO Casida formulation of TD-DFT<sup>43</sup> and the LCAO time propagation (TP) TD-DFT code.<sup>12</sup> In the Casida approach, the matrix eigenvalue equation,<sup>43</sup>

$$\boldsymbol{\Omega}\mathbf{F}_I = \omega_I^2\mathbf{F}_I \quad (1)$$

is solved to yield the excitation energies,  $\omega_I$  and corresponding Casida eigenvectors,  $\mathbf{F}_I$ . The matrix  $\boldsymbol{\Omega}$  is constructed in electron-hole space such that the KS excitations from an initially occupied state,  $i$  ( $j$ ), to an initially unoccupied state,  $a$  ( $b$ ), are written as<sup>8</sup>

$$\Omega_{ia,jb} = \omega_{ia}^2 \delta_{ia,jb} + 2\sqrt{f_{ia}\omega_{ia}}\lambda K_{ia,jb}\sqrt{f_{jb}\omega_{jb}} \quad (2)$$

where  $f_{ia} = f_a - f_i$  is the occupation number difference,  $\omega_{ia} = \varepsilon_a - \varepsilon_i$  is the KS eigenvalue difference, and  $K_{ia,jb}$  represents the first order interaction (“coupling”) between the excitations  $i \rightarrow a$  and  $j \rightarrow b$ . The dimensionless scaling factor,  $\lambda$ , provides a transformation from the non-interacting framework at  $\lambda = 0$  to the fully-interacting framework at  $\lambda = 1$ .

In the TP TD-DFT approach,<sup>12</sup> the electron wavefunctions are evolved after an initial external electric (in dipole approximation)  $\delta$ -pulse<sup>44</sup> along the long wire axis. The time-dependent induced density provides the time-dependent dipole moment from which the dynamical polarizability and the ensuing frequency-dependent photoabsorption spectrum are determined. The photoabsorption spectrum with Gaussian broadening of  $\sigma = 0.07$  eV is sufficiently obtained using a time step of 10 as for a total propagation time of 30 fs. The non-interacting spectra were calculated with a distinct time propagation and interaction strength parameter ( $\lambda$ ) equal to 0.

The optical spectrum from the Casida formulation was equivalent to the spectrum calculated using the TP method with full interaction. The Casida implementation efficiently computes the photoabsorption spectra with a variable interaction parameter<sup>7</sup> without requiring several distinct  $\lambda$ -dependent calculations as in time propagation methods. The Gaussian broadening of the spectra calculated within the Casida formulation is  $\sigma = 0.04$  eV.

Both for the Casida and TP formulations of TD-DFT, the induced density matrix between occupied and unoccupied KS states and the corresponding dipole matrix elements allows the photoabsorption spectrum to be decomposed into contributions from individual discrete electron-hole transitions.<sup>8,45,46</sup> The different discrete electron-hole transitions are denoted by spots on a two-dimensional map (cf. Figure 2A) with an intensity proportional to the normalized photoabsorption decomposition weight of the KS electron-hole transition ( $S_{ia}/S$ ) (see eqn. 17 and 21 in Ref<sup>8</sup>). The red (blue) color of the spots corresponds to the positive (negative) sign of the photoabsorption decomposition of the transition. The extent is given by a two-dimensional Gaussian broadening function ( $\sigma_{TCM} = 0.04$  eV) and is distinct from the broadening of the photoabsorption spectrum,  $\sigma$ . In this report, the initially unoccupied and initially occupied energies,  $\varepsilon_u$  and  $\varepsilon_o$ , and Density of States (DOS) are given on the vertical and horizontal axes of TCM, respectively. The photoabsorption energy is noted as  $\omega$  and spots on the line  $\omega = \varepsilon_u - \varepsilon_o$  correspond to the electron-hole transitions which are not affected by the Coulomb and exchange-correlation kernel interactions. The induced density can be decomposed into partial densities corresponding to the different electron-hole transition contributions. Further theoretical details about these analysis tools can be found elsewhere.<sup>8</sup>

Some of the nanowire systems were also calculated using Gaussian 03<sup>24</sup> with a B3PW91 hybrid functional<sup>25–27</sup> and a LanL2DZ basis set.<sup>28</sup> The main features of the photoabsorption spectra were consistent with GLLB-SC exchange-correlation potential.<sup>47</sup>

## Acknowledgement

The work was supported in part by US DOE Grant DE-FG02-07ER46354 (NN, VT, and TSR) and as part of the Academy of Finland Centre of Excellence program (project 251748, KMC, TPR, and MJP and project 312298, KMC). TPR also acknowledges support from the Knut and Alice Wallenberg Foundation and the Swedish Research Council. MK acknowledges funding from Academy of Finland under grant Nr. 295602. We acknowledge computational resources provided

by CSC – IT Center for Science (Finland) and by the Aalto Science-IT project (Aalto University School of Science).

## References

1. Bohm, D.; Pines, D. A collective description of electron interactions: III. Coulomb interactions in a degenerate electron gas. *Phys. Rev.* **1953**, *92*, 609.
2. Iida, K.; Noda, M.; Ishimura, K.; Nobusada, K. First-principles computational visualization of localized surface plasmon resonance in gold nanoclusters. *J. Phys. Chem. A* **2014**, *118*, 11317–11322.
3. Koval, P.; Marchesin, F.; Foerster, D.; Sánchez-Portal, D. Optical response of silver clusters and their hollow shells from linear-response TDDFT. *J. Phys. Condens. Matter* **2016**, *28*, 214001.
4. Ma, J.; Wang, Z.; Wang, L.-W. Interplay Between Plasmon and Single-Particle Excitations in a Metal Nanocluster. *Nat. Commun.* **2015**, *6*, 10107.
5. Kumar, P. V.; Rossi, T. P.; Kuiska, M.; Erhart, P.; Norris, D. J. Direct hot-carrier transfer in plasmonic catalysis. *Faraday Discuss.* **2019**, *214*, 189–197.
6. Ma, J.; Gao, S. Plasmon Induced Electron-Hole Separation at the Ag/TiO<sub>2</sub> (110) Interface. *ACS Nano* **2019**,
7. Bernadotte, S.; Evers, F.; Jacob, C. R. Plasmons In Molecules. *J. Phys. Chem. C* **2013**, *117*, 1863–1878.
8. Rossi, T. P.; Kuiska, M.; Puska, M. J.; Nieminen, R. M.; Erhart, P. Kohn–Sham Decomposition in Real-Time Time-Dependent Density-Functional Theory: An Efficient Tool for Analyzing Plasmonic Excitations. *J. Chem. Theory Comput.* **2017**, *13*, 4779–4790.

9. Zhang, R.; Bursi, L.; Cox, J. D.; Cui, Y.; Krauter, C. M.; Alabastri, A.; Manjavacas, A.; Calzolari, A.; Corni, S.; Molinari, E.; Carter, E. A.; de Abajo, F. J. G.; Zhang, H.; Nordlander, P. How to Identify Plasmons from the Optical Response of Nanostructures. *ACS Nano* **2017**, *11*, 7321–7335.
10. de Abajo, F. J. G.; Sapienza, R.; Noginov, M.; Benz, F.; Baumberg, J.; Maier, S.; Graham, D.; Aizpurua, J.; Ebbesen, T.; Pinchuk, A.; Khurgin, J.; Matczyszyn, K.; Hugall, J. T.; van Hulst, N.; Dawson, P.; Roberts, C.; Nielsen, M.; Bursi, L.; Flatté, M.; Yi, J. *et al.* Plasmonic and New Plasmonic Materials: General Discussion. *Faraday Discuss.* **2015**, *178*, 123–149.
11. Manjavacas, A.; Marchesin, F.; Thongrattanasiri, S.; Koval, P.; Nordlander, P.; Sanchez-Portal, D.; de Abajo, F. J. G. Tunable molecular plasmons in polycyclic aromatic hydrocarbons. *ACS Nano* **2013**, *7*, 3635–3643.
12. Kuisma, M.; Sakkola, A.; Rossi, T. P.; Larsen, A. H.; Enkovaara, J.; Lehtovaara, L.; Rantala, T. T. Localized Surface Plasmon Resonance in Silver Nanoparticles: Atomistic First-Principles Time-Dependent Density-Functional Theory Calculations. *Phys. Rev. B* **2015**, *91*, 115431.
13. Rossi, T. P.; Shegai, T.; Erhart, P.; Antosiewicz, T. J. Strong plasmon-molecule coupling at the nanoscale revealed by first-principles modeling. *Nat. Commun.* **2019**, *10*, 3336.
14. Rossi, T. P.; Winther, K. T.; Jacobsen, K. W.; Nieminen, R. M.; Puska, M. J.; Thygesen, K. S. Effect of Edge Plasmons on the Optical Properties of MoS<sub>2</sub> Monolayer Flakes. *Phys. Rev. B* **2017**, *96*, 155407.
15. Conley, K. M.; Nayyar, N.; Rossi, T. P.; Kuisma, M.; Turkowski, V.; Puska, M. J.; Rahaman, T. S. Plasmon Excitations in Mixed Metallic Nanoarrays. *ACS Nano* **2019**, *13*, 5344–5355.
16. Kümmel, S.; Andrae, K.; Reinhard, P.-G. Collectivity in the Optical Response of Small Metal Clusters. *Appl. Phys. B: Lasers Opt.* **2001**, *73*, 293–297.

17. Casanova, D.; Matxain, J. M.; Ugalde, J. M. Plasmonic resonances in the Al<sub>13</sub>–cluster: Quantification and origin of exciton collectivity. *J. Phys. Chem. C* **2016**, *120*, 12742–12750.
18. Malola, S.; Kaappa, S.; Hakkinen, H. Role of Nanocrystal Symmetry in the Crossover Region from Molecular to Metallic Gold Nanoparticles. *J. Phys. Chem. C* **2019**, *123*, 20655–20663.
19. Wang, B.-J.; Xu, Y.; Ke, S.-H. Plasmon Excitations in Sodium Atomic Planes: A Time-Dependent Density Functional Theory Study. *J. Chem. Phys.* **2012**, *137*, 054101.
20. Yin, H.-F.; Zhang, H. Collectivity of Plasmon Excitations in Small Sodium Clusters with Planar Structure. *Phys. B (Amsterdam, Neth.)* **2012**, *407*, 416–420.
21. Krauter, C. M.; Bernadotte, S.; Jacob, C. R.; Pernpointner, M.; Dreuw, A. Identification of Plasmons in Molecules with Scaled *ab initio* Approaches. *J. Phys. Chem. C* **2015**, *119*, 24564–24573.
22. Guidez, E. B.; Aikens, C. M. Origin and TDDFT benchmarking of the plasmon resonance in acenes. *J. Phys. Chem. C* **2013**, *117*, 21466–21475.
23. Guidez, E. B.; Aikens, C. M. Quantum Mechanical Origin of the Plasmon: From Molecular Systems to Nanoparticles. *Nanoscale* **2014**, *6*, 11512–11527.
24. Frisch, M. J.; Trucks, G. W.; Schlegel, H. B.; Scuseria, G. E.; Robb, M. A.; Cheeseman, J. R.; Montgomery, J. A., Jr.; Vreven, T.; Kudin, K. N.; Burant, J. C.; Millam, J. M.; Iyengar, S. S.; Tomasi, J.; Barone, V.; Mennucci, B.; Cossi, M.; Scalmani, G.; Rega, N.; Petersson, G. A.; Nakatsuji, H. *et al.* Gaussian 03, Revision D.01. Gaussian, Inc., Wallingford, CT, 2004.
25. Becke, A. D. Density-Functional Thermochemistry. III. The Role of Exact Exchange. *J. Chem. Phys.* **1993**, *98*, 5648–5652.
26. Perdew, J. P.; Yue, W. Accurate and Simple Density Functional for the Electronic Exchange Energy: Generalized Gradient Approximation. *Phys. Rev. B* **1986**, *33*, 8800.

27. Perdew, J. P. Electronic Structure of Solids, Eds. P. Ziesche and H. Eschrig. Berlin: Academic, 1991.
28. Hay, P. J.; Wadt, W. R. *Ab initio* Effective Core Potentials for Molecular Calculations. Potentials for K to Au Including the Outermost Core Orbitals. *J. Chem. Phys.* **1985**, *82*, 299–310.
29. Mortensen, J. J.; Hansen, L. B.; Jacobsen, K. W. Real-Space Grid Implementation of the Projector Augmented Wave Method. *Phys. Rev. B* **2005**, *71*, 035109.
30. Enkovaara, J.; Rostgaard, C.; Mortensen, J. J.; Chen, J.; Dułak, M.; Ferrighi, L.; Gavnholt, J.; Glinsvad, C.; Haikola, V.; Hansen, H. A.; Kristoffersen, H. H.; Kuisma, M.; Larsen, A. H.; Lehtovaara, L.; Ljungberg, M.; Lopez-Acevedo, O.; Moses, P. G.; Ojanen, J.; Olsen, T.; Petzold, V. *et al.* Electronic Structure Calculations with GPAW: A Real-Space Implementation of the Projector Augmented-Wave Method. *J. Phys.: Condens. Matter* **2010**, *22*, 253202.
31. Walter, M.; Häkkinen, H.; Lehtovaara, L.; Puska, M.; Enkovaara, J.; Rostgaard, C.; Mortensen, J. J. Time-Dependent Density-Functional Theory in the Projector Augmented-Wave Method. *J. Chem. Phys.* **2008**, *128*, 244101.
32. Yannouleas, C.; Broglia, R. A.; Brack, M.; Bortignon, P. F. Fragmentation of the Photoabsorption Strength in Neutral and Charged Metal Microclusters. *Phys. Rev. Lett.* **1989**, *63*, 255–258.
33. Nayyar, N.; Turkowski, V.; Rahman, T. S. Optical Generation of Collective Plasmon Modes in Small Gold Chains Induced by Doping Transition-Metal Impurities. *Phys. Rev. Lett.* **2012**, *109*, 157404.
34. Nilius, N.; Wallis, T.; Ho, W. Development of One-Dimensional Band Structure in Artificial Gold Chains. *Science* **2002**, *297*, 1853–1856.
35. Hohenberg, P.; Kohn, W. Inhomogeneous Electron Gas. *Phys. Rev.* **1964**, *136*, B864–B871.
36. Kohn, W.; Sham, L. J. Self-Consistent Equations Including Exchange and Correlation Effects. *Phys. Rev.* **1965**, *140*, A1133–A1138.

37. Kuisma, M.; Ojanen, J.; Enkovaara, J.; Rantala, T. T. Kohn-Sham Potential with Discontinuity for Band Gap Materials. *Phys. Rev. B* **2010**, *82*, 115106.
38. Yan, J.; Jacobsen, K. W.; Thygesen, K. S. First-Principles Study of Surface Plasmons on Ag(111) and H/Ag(111). *Phys. Rev. B* **2011**, *84*, 235430.
39. Yan, J.; Jacobsen, K. W.; Thygesen, K. S. Conventional and Acoustic Surface Plasmons on Noble Metal Surfaces: A Time-Dependent Density Functional Theory Study. *Phys. Rev. B* **2012**, *86*, 241404.
40. Blöchl, P. E. Projector Augmented-Wave Method. *Phys. Rev. B* **1994**, *50*, 17953–17979.
41. Larsen, A. H.; Mortensen, J. J.; Blomqvist, J.; Castelli, I. E.; Christensen, R.; Dułak, M.; Friis, J.; Groves, M. N.; Hammer, B.; Hargus, C.; Hermes, E. D.; Jennings, P. C.; Jensen, P. B.; Kermode, J.; Kitchin, J. R.; Kolsbjerg, E. L.; Kubal, J.; Kaasbjerg, K.; Lysgaard, S.; Maronsson, J. B. *et al.* The Atomic Simulation Environment—A Python Library for Working with Atoms. *J. Phys.: Condens. Matter* **2017**, *29*, 273002.
42. Larsen, A. H.; Vanin, M.; Mortensen, J. J.; Thygesen, K. S.; Jacobsen, K. W. Localized Atomic Basis Set in the Projector Augmented Wave Method. *Phys. Rev. B* **2009**, *80*, 195112.
43. Casida, M. E. In *Recent Advances in Density Functional Methods, Part I*; Chong, D. P., Ed.; World Scientific, Singapore, 1995; p 155.
44. Yabana, K.; Bertsch, G. F. Time-dependent Local-Density Approximation in Real Time. *Phys. Rev. B* **1996**, *54*, 4484–4487.
45. He, Y.; Zeng, T. First-Principles Study and Model of Dielectric Functions of Silver Nanoparticles. *J. Phys. Chem. C* **2010**, *114*, 18023–18030.
46. Malola, S.; Lehtovaara, L.; Enkovaara, J.; Häkkinen, H. Birth of the Localized Surface Plasmon Resonance in Monolayer-Protected Gold Nanoclusters. *ACS Nano* **2013**, *7*, 10263–10270.

47. Nayyar, N. Optical and Magnetic Properties of Nanostructures. Ph.D. thesis, University of Central Florida, 2014.